Chemical Engineering Journal 435 (2022) 134795

Contents lists available at ScienceDirect

Chemical Engineering Journal

journal homepage: www.elsevier.com/locate/cej

Interface engineering of $Co_2N_{0.67}/CoMoO_4$ heterostructure nanosheets as a highly active electrocatalyst for overall water splitting and Zn-H_2O cell

Yan Hu [a,1], Zuyang Luo [a,1], Man Guo [a], Jiaxin Dong [a], Puxuan Yan [a], Chuan Hu [a], Tayirjan Taylor Isimjan [b,*], Xiulin Yang [a,*]

[a] Guangxi Key Laboratory of Low Carbon Energy Materials, School of Chemistry and Pharmaceutical Sciences, Guangxi Normal University, Guilin 541004, China
[b] Saudi Arabia Basic Industries Corporation (SABIC) at King Abdullah University of Science and Technology (KAUST), Thuwal 23955-6900, Saudi Arabia

ARTICLE INFO

Keywords:
$Co_2N_{0.67}/CoMoO_4$
Heterostructures
Water splitting
Zn-H_2O cell
Theoretical calculations

ABSTRACT

The key in developing a low-cost, high-efficiency electrocatalyst for hydrogen generation is not only cutting the cost by avoiding noble metals but also utilizing the structure–function relationship to expose the maximum amounts of active sites on the surface by increasing the interface between the active components. Here, we demonstrated full-cycle synthesis, characterization, and optimization of $Co_2N_{0.67}/CoMoO_4$ electrocatalyst on carbon-supported by density functional theory (DFT) calculations. The DFT calculation revealed a significant charge accumulation at the interface between $Co_2N_{0.67}$ and $CoMoO_4$, suggesting the possibility of a strong synergy. As expected, electrochemical studies have shown a bifunctional $Co_2N_{0.67}/CoMoO_4$ catalyst with low overpotential and durability towards hydrogen/oxygen evolution reactions (HER/OER) in alkaline electrolytes and robust overall water splitting performance at high current densities. In addition, the optimized $Co_2N_{0.67}/CoMoO_4$ catalyst is also used in a Zn-H_2O cell and displayed a power density exceeding Pt/C with the long-term stability of up to 170 h. The excellent electrochemical performance is the outcome of the better charge mobility at the interface resulted in the unique synergy between the active components.

1. Introduction

Electrochemical water splitting is considered to be the cleanest and sustainable method for high-quality hydrogen production that heavily depends on catalysts to facilitate H_2 generation and subsequent utilization [1–3]. The key challenges in catalyst development are to overcome the slow reaction kinetics resulted from high overpotential [4–8]. Moreover, large-scale H_2 production to grid-level requires catalysts that are easy to prepare, cheap, and comparable to the state-of-the-art noble-metal-based catalysts [9–13]. Therefore, the development of low-cost, high-efficiency transition metal-based hydrogen fuel catalysts is of great significance [14].

In the past few decades, significant progress has been made in utilizing transition metal alloys and metallic compounds such as sulfides [15,16], phosphides [17,18], nitride compounds [19–22], borides [23,24], oxides [25] etc., as potential electrocatalysts for water splitting. Among all of these materials, transition metal nitrides and oxides exhibit great potential due to their excellent electrical conductivity and corrosion resistance [26–28]. Although few heterogeneous interfaces about transition metal nitrides and oxides have been reported, the designed catalysts still possess relatively high overpotentials that hinder their further application. As an emerging new strategy, interface engineering creates interfacial synergy through optimizing the electronic structure and thereby improves the catalytic activity of water splitting [11,18,29]. Hu et al. reported a heterostructure catalyst of $Ni_3N/Ni_{0.2}Mo_{0.8}N$ microspheres that exhibited high HER and OER performances by establishing abundant interfaces between two components [30]. Afterwards, Cao et al. demonstrated a multifunctional Mo-doped $NiCo_2O_4/Co_{5.47}N$ heterostructure electrocatalyst that presented remarkable catalytic activity toward the OER (η_{50} = 310 mV) and HER (η_{50} = 170 mV), respectively [31]. Obviously, bifunctionality permits the cost reduction plus intrinsic stability that extends the catalysts lifetime through in situ electrochemical regeneration by bias-switching [32,33]. Furthermore, the bifunctionality also hints at the structure–function further guiding the process parameters toward the optimal points [34]. Nevertheless, there are still rooms to improve the catalyst

* Corresponding authors.
E-mail addresses: isimjant@sabic.com (T.T. Isimjan), xlyang@gxnu.edu.cn (X. Yang).
[1] These authors contributed equally.

https://doi.org/10.1016/j.cej.2022.134795
Received 14 October 2021; Received in revised form 31 December 2021; Accepted 16 January 2022
Available online 20 January 2022

performance and stability especially at high current densities (>100 mA cm^{-2}) [35–37]. Regulating the morphology of catalyst to maximize the active site utilization is feasible through a rational design and unique preparation method, especially stereo-assembly of the heterostructure. Additionally, contrary to the electrochemical water splitting that requires additional energy to generate H_2, the Zn-H_2O fuel cell is capable of simultaneous hydrogen production and electricity generation using the energy generated from Zn oxidation [38,39]. However, transition metal-based nitrides have not yet been explored in Zn-H_2O fuel cells.

In this work, the hetero-structured $Co_2N_{0.67}$/$CoMoO_4$ nanoparticles electrocatalysts were *in-situ* assembled on CC to forming nanosheet through a simple ion-exchange hydrothermal process followed by nitriding treatment. The microstructure and chemical state of the catalysts were characterized and analyzed. XRD and TEM proved the existence of $Co_2N_{0.67}$ and $CoMoO_4$ crystals and the formation of heterogeneous interfaces. The electrochemical performance of the catalyst in an alkaline medium was further studied. The experimental results show that the $Co_2N_{0.67}$/$CoMoO_4$ catalyst requires overpotentials of only 63 mV (HER) and 283 mV (OER) to drive the current density of 10 mA cm^{-2}, respectively. Furthermore, the $Co_2N_{0.67}$/$CoMoO_4$ catalyst used as a cathode in alkaline Zn–H_2O fuel cell and displayed a power density of up to 20 mW cm^{-2} and superior to that of commercial Pt/C (10.5 mW cm^{-2}) under the same condition. More importantly, the $Co_2N_{0.67}$/$CoMoO_4$ reveals robust stability of keeping 170 h for H_2 generation. Theoretical calculations demonstrate that the synergy between $Co_2N_{0.67}$ and $CoMoO_4$ components at the interface can reduce the energy barrier of reaction intermediates, and facilitate the release of H_2 and O_2, thereby improving the catalytic activity. This study is focused on the overall performance and the cost-effectiveness of bifunctional catalyst. Moreover, the scalability and stability at high current density for actual industrial application. The studies on the heterojunction of cobalt-molybdenum metal nitrides and oxides have been rare, especially as a dual-function electrocatalyst for the HER and OER. Finally, the $Co_2N_{0.67}$/$CoMoO_4$ synthesized by the ion exchange hydrothermal method has a nanosheet structure composed of nanoparticles that creates a sufficient heterogeneous interface, thereby better performance.

2. Experimental details

2.1. Materials

Cobalt nitrate hexahydrate ($Co(NO_3)_2{\cdot}6H_2O$, 99.0%), sodium molybdate dehydrate ($Na_2MoO_4{\cdot}2H_2O$, 99.0%), urea (CH_4N_2O, ≥99.0%) were analytical reagents and used without further purification. Commercial Pt/C (20 wt% for platinum) was purchased from Alfa Aesar.

2.2. Synthesis of CoCH/CC nanosheets

Typically, $Co(NO_3)_2{\cdot}6H_2O$ (2 mmol) and urea (10 mmol) were dissolved in 35 mL water under continuously stirring for 30 min. The solution was transferred to a 50 mL autoclave lined with polytetrafluoroethylene, and the cleaned carbon cloth (CC) was placed in the autoclave at an angle. The autoclave was then sealed and heated at 120 °C for 6 h. After cooling, the sample of $Co(CO_3)_{0.5}(OH)_{0.11}{\cdot}H_2O$/CC (CoCH/CC) was taken out and thoroughly washed with water and ethanol and then dried at 60 °C (loading: 1.4 mg cm^{-2}).

2.3. Synthesis of CoCH/$CoMoO_4$ nanosheets on CC

By changing the amount of $Na_2MoO_4{\cdot}2H_2O$ (100, 150, and 200 mg mL^{-1}), CoCH/$CoMoO_4$ samples with different Mo content were prepared. Using a similar hydrothermal method, $Na_2MoO_4{\cdot}2H_2O$ was dissolved in 35 mL of water. After continuous stirring for 30 min, the solution was transferred to a 50 mL autoclave lined with polytetrafluoroethylene. The precursor CoCH/CC was placed in the autoclave at an angle and heated at 130 °C for 6 h. Similarly, after cooling, the coach/$CoMoO_4$ was taken out and washed with water and ethanol thoroughly, and dried overnight (loading: 2.3 mg cm^{-2}).

2.4. Synthesis of $Co_2N_{0.67}$/$CoMoO_4$ nanosheets on CC ($Co_2N_{0.67}$/$CoMoO_4$)

The obtained CoCH/$CoMoO_4$ was placed in a tube furnace and annealed at 400 °C for 5 h with a ramp rate of 5 °C min^{-1} under a flow of ammonia gas, respectively. The obtained sample was denoted as $Co_2N_{0.67}$/$CoMoO_4$ (loading: 2.1 mg cm^{-2}).

2.5. Synthesis of $Co_2N_{0.67}$ nanosheets on CC ($Co_2N_{0.67}$/CC)

The obtained CoCH was placed in a tube furnace and annealed at 400 °C for 5 h with a ramp rate of 5 °C min^{-1} under a flow of ammonia gas. The obtained sample was denoted as $Co_2N_{0.67}$.

2.6. Synthesis of $CoMoO_4$ nanosheets on CC ($CoMoO_4$/CC)

The synthesis process of $CoMoO_4$/CC is similar to that of CoCH/CC, except that urea (10 mmol) is replaced by $Na_2MoO_4{\cdot}2H_2O$ (2 mmol). The obtained product was placed in a tube furnace and annealed at 350 °C for 2 h with a ramp rate of 5 °C min^{-1} under a flow of nitrogen gas.

2.7. Synthesis of RuO_2 and 20 wt% Pt/C electrodes

The $RuCl_3{\cdot}3H_2O$ was directly calcined at 400 °C for 3 h in the air to obtain RuO_2 powders. And then 2 mg RuO_2 or 20 wt% commercial Pt/C was dispersed into a mixture of 100 μL deionized water, 100 μL ethanol and 5 μL 5 wt% Nafion, respectively. The mixture was ultrasonically treated for at least 30 min to form a uniform catalyst ink, then dropped onto the surface of CC (1 cm × 1 cm) and dried naturally in the air. The corresponding XRD pattern are indexed to RuO_2 (JCPDS: 40–1290), confirming the successful preparation of RuO_2. The SEM image indicates that RuO_2 exists in the form of particles (Fig. S2).

2.8. Electrochemical measurements

The electrocatalytic activity was performed on a Biologic VMP3 electrochemical work station with a standard three-electrode system in alkaline. The catalysts, graphite plate, and calomel electrode were used as working, counter and reference electrodes, respectively. The cyclic voltammetry (CV) test was performed with a sweep rate of 5 mV s^{-1} at a potential of − 0.9 to − 1.5 V and 0 to 0.8 V for HER and OER, respectively. Linear sweep voltammetry (LSV) was carried out at a scan rate of 1 mV s^{-1}, and the electrochemical impedance spectroscopy (EIS) measurements were performed near the onset potential in the frequency range from 200 kHz to 10 mHz. The potential of E_{RHE} was calibrated by the equation of $E_{RHE} = E_{SCE} + 0.241 + 0.059$ pH, consistent with the calibration results of the standard hydrogen electrode (RHE) (Fig. S1). All the LSV polarization curves were corrected against *iR* compensation. The electrochemical double-layer capacitance (C_{dl}) measured by cyclic voltammetry at different scan rates (1, 2, 4, 6, 8, 10 mV s^{-1}) to estimate the electrochemically active surface area (ECSA). The overall water splitting test was performed by a two-electrode system in the potential range of 0 ~ 2.0 V with a scan rate of 5 mV s^{-1} in 1.0 M KOH solution.

2.9. Zn-H_2O cell measurements

The Zn-H_2O cell was assembled according to the following process: typically, the cathode electrode was a CC (1 × 1 cm^2) loaded with $Co_2N_{0.67}$/$CoMoO_4$ catalyst (2.1 mg). Then a polished zinc foil was used as the anode, 6 mol L^{-1} KOH and 0.2 mol L^{-1} $Zn(Ac)_2$ were used as an electrolyte, and the electrolyte was saturated with N_2 before the test for suppressing the oxygen reduction reaction. For comparison, 2.1 mg Pt/C

catalyst ink was prepared by loading on a 1 × 1 cm^2 CC (the catalyst was mixed with 5% Nafion solution and water/isopropanol solution (1:3 (v/v)) to prepare catalyst ink). All electrochemical tests were conducted on electrochemical workstation (CHI 760E) under ambient conditions. The stability was tested by using the LAND battery testing system (BT2016A) at a current density of 5 mA cm^{-1} with 20 min per cycle (10 min charge and 10 min discharge). The specific capacity was calculated from the following equation:

$$specific\ capacity = \frac{discharge\ current \times time}{weight\ of\ consumed\ Zinc}$$

3. Results and discussion

3.1. Synthesis strategy and structural analysis

The fabrication processes of hierarchical $Co_2N_{0.67}/CoMoO_4$ nanosheets are a three-step route, as shown in Fig. 1a. The Co$(CO_3)_{0.5}(OH)_{0.11}{\cdot}H_2O$ (CoCH) nanosheets precursor on the CC was first prepared by a hydrothermal method followed by a hydrothermal ion-exchange process to make $CoCH/CoMoO_4$ nanosheets, which were further processed under NH_3 atmosphere at 400 °C to generate the final composite of $Co_2N_{0.67}/CoMoO_4$. The corresponding SEM image shows uniform distribution of nanosheet arrays on the CC surface after the hydrothermal process (Fig. S3a), and the X-ray diffraction (XRD) patterns is indexed to CoCH (JCPDS: 48–0083) (Fig. 1b) [18], which showed a stable morphology after the consecutive hydrothermal treatment (Fig. S3b). However, an additional $CoMoO_4$ crystal phase (JCPDS: 25–1434) (Fig. S4b) appeared, indicating the formation of $CoMoO_4$ species through the ion exchange process.

As shown in Fig. 1b, the XRD pattern indicated that the CoCH characteristics diffraction peaks disappeared completely after ammonia treatment at 400 °C. In contrast, the characteristic diffraction peak of $Co_2N_{0.67}$ (JCPDS: 06–0691) was observed, confirming that CoCH has been converted to $Co_2N_{0.67}$ [40]. Both the CoCH and $Co_2N_{0.63}/CoMoO_4$ samples show a prominent carbon peak between 20 and 30°. The characteristic diffraction peak of molybdenum nitride isn't detected since molybdenum nitride formation requires a much higher temperature (~700 °C), and the catalysts were prepared at 400 °C in this study corresponding obvious peaks at 14.2, 28.5, 43.4, 59.6, 61.2, and 62.8° can index well with $CoMoO_4$ (JCPDS: 25–1434) [41]. The control

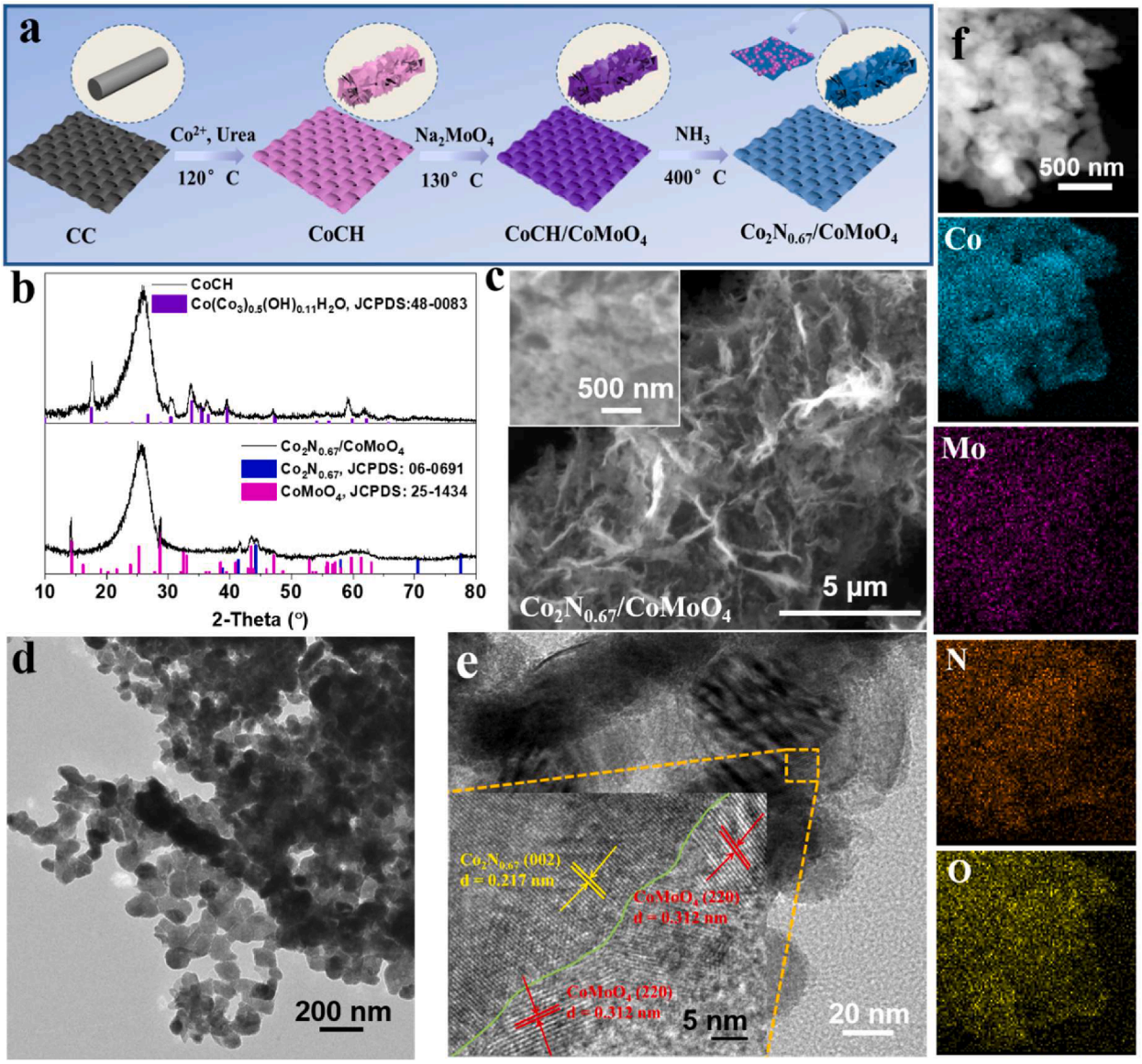

Fig. 1. (a) Schematic illustration of the synthesis of $Co_2N_{0.67}/CoMoO_4$. (b) XRD patterns of CoCH and $Co_2N_{0.67}/CoMoO_4$. (c) SEM images of $Co_2N_{0.67}/CoMoO_4$. (d) TEM image, (e) High-resolution TEM image, and (f) HAADF-STEM image and corresponding elemental mappings of $Co_2N_{0.67}/CoMoO_4$ (color online).

experiment (nitriding the CoCH precursor and hydrothermal of $CoNO_3$ and $NaMoO_4$) also displayed the formation of the $Co_2N_{0.67}$ and $CoMoO_4$ crystal phase, respectively (Fig. S4a and S4c). The SEM image indicated that $Co_2N_{0.67}/CoMoO_4$ maintained the nanosheet structure after annealing, except that the surface of the nanosheet became rough in virtue of ammonia etching (Fig. 1c). The N_2 adsorption/desorption isotherm of $Co_2N_{0.67}/CoMoO_4$ displays a typical type III behavior and the Brunauer-Emmett-Teller (BET) surface area of 27.5 $m^2\ g^{-1}$. Barrett-Joyner-Halenda (BJH) pore size distribution curve (Fig. S4d) reveals that $Co_2N_{0.67}/CoMoO_4$ has a mesoporous structure with a pore size of about 3.8 nm.

The high-resolution SEM and transmission electron microscopy (TEM) images displayed that the nanosheet of the $Co_2N_{0.67}/CoMoO_4$ is composed of numerous nanoparticles with average particles size of 100 nm at high resolution (Fig. 1d) [42,43]. As shown in the high-resolution TEM image of Fig. 1e, one of the noticeable lattice spacings of 0.217 nm corresponds to the (0 0 2) crystal plane of $Co_2N_{0.67}$, and the $d = 0.312$ nm is corresponding to the (2 2 0) crystal plane of $CoMoO_4$. Interestingly, the apparent grain boundaries at high magnification were not reflected on lower resolution elemental mapping, consistent with other reports [2,44,45]. Moreover, there is an observable interface between the $Co_2N_{0.67}$ and $CoMoO_4$ crystal phases, indicating the existence of heterostructures. The corresponding element mapping images of $Co_2N_{0.67}/CoMoO_4$ (Fig. 1f) reveal the uniform distribution of Co, Mo, N, and O throughout the catalyst.

3.2. Chemical state analysis

X-ray photoelectron spectroscopy (XPS) was used to study the surface electronic valence and chemical composition. As shown in Fig. S5a, the XPS spectrum shows that the surface of $Co_2N_{0.67}/CoMoO_4$ is mainly composed of Co, Mo, N, and O elements. The high-resolution C 1 s spectrum is deconvoluted into four peaks at 284.0 (C═C), 284.8 (C–C) and 285.3 eV (C–N) and 286.1 eV (C-O) (Fig. S5b) [46,47]. The Co (II) and Mo (Vl) peaks are observed in the oxide samples (Fig. 2a, b). The peaks at 779.4 and 781.3 eV in Co $2p_{2/3}$ region can be attributed to Co-N and Co(II),respectively. (Fig. 2a) [26,40]. There is a strong Co-N peak that appeared in $Co_2N_{0.67}/CoMoO_4$ after NH_3 treatment indicates N doping. The high-resolution XPS spectrum of Mo 3*d* of $Co_2N_{0.67}/CoMoO_4$ and $CoCH/CoMoO_4$ are shown in Fig. 2b. The peak at 232.6 eV is assigned to Mo (Vl) of $CoMoO_4$ [46,48]. Obviously, the content of Co^{2+} is increasing with the introduction of Mo, confirming that $Co_2N_{0.67}/CoMO_4$ possesses more active sites [49]. The N 1 s spectrums are shown in Fig. 2c. The peaks at 397.5 and 398.7 eV are assigned to the Co-N and pyridinic-N of the $Co_2N_{0.67}/CoMoO_4$ sample [4,50]. Meanwhile, the O 1 s spectrum is deconvoluted into three peaks at 530.2, 531.8, and 533.0 eV assigned to the Metal-O, O-vacancies and absorbed O species from $Co_2N_{0.67}/CoMoO_4$, respectively (Fig. 2d) [51,52].

3.3. Electrocatalytic HER analysis

The HER behavior of the catalysts with an area of 1 × 1 cm was measured using a standard three-electrode system in 1.0 M KOH at a scan rate of 2 mV s^{-1} (Fig. S6). As shown in Fig. 3a-b, the $Co_2N_{0.67}/CoMoO_4$ catalyst showed an HER overpotential of 63 mV@10 mA cm^{-2}, which is comparable to that of the commercial Pt/C. Whereas, it only requires 315 mV to reach 1000 mA cm^{-2}, indicating a high potential for industrial applications. As expected, $Co_2N_{0.67}/CoMoO_4$ displayed better electrocatalytic activity that surpassed those of $CoMoO_4$, CoCH, $Co_2N_{0.67}$, $CoCH/CoMoO_4$ catalysts, and other similar transition metal-based catalysts (Table S2). Generally, the HER kinetic and the rate-determining steps are investigated by Tafel plots. The Tafel slope of $Co_2N_{0.67}/CoMoO_4$ was 57.5 mV dec^{-1}, lower than those of CoCH (153.5 mV dec^{-1}), $CoMoO_4$ (175.2 mV dec^{-1}), $Co_2N_{0.67}$ (127.8 mV dec^{-1}), and $CoCH/CoMoO_4$ (146.7 mV dec^{-1}), revealing a Volmer–Heyrovsky reaction pathway is the rate-determining step for $Co_2N_{0.67}/CoMoO_4$ (Fig. 3c) [18,46]. Further, EIS results demonstrated that the $Co_2N_{0.67}/CoMoO_4$ displayed the lowest charge-transfer resistance (R_{ct}) among all simples except Pt/C, implying a fast charge transfer mechanism (Fig. S7). Particularly, XRD patterns confirmed that as prepared samples different Na_2MoO_4 concentration have similar composite structure of $Co_2N_{0.67}$ and $CoMoO_4$ (Fig. S8). The LSV curve shows that $Co_2N_{0.67}/$

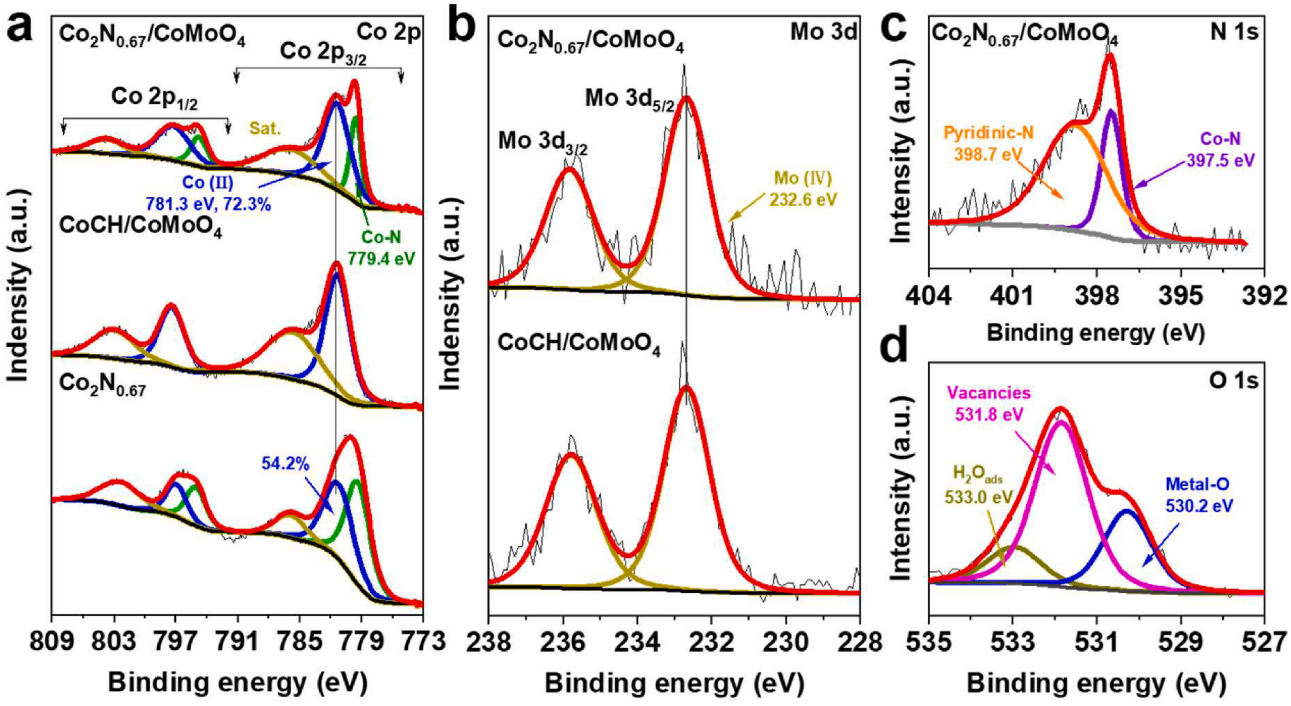

Fig. 2. High-resolution XPS spectra of (a) Co 2p from $Co_2N_{0.67}/CoMoO_4$, $CoCH/CoMoO_4$ and $Co_2N_{0.67}$. (b) Mo 3d regions from $Co_2N_{0.67}/CoMoO_4$ and $CoCH/CoMoO_4$, respectively. (c) N 1 s and (d) O 1 s regions from $Co_2N_{0.67}/CoMoO_4$.

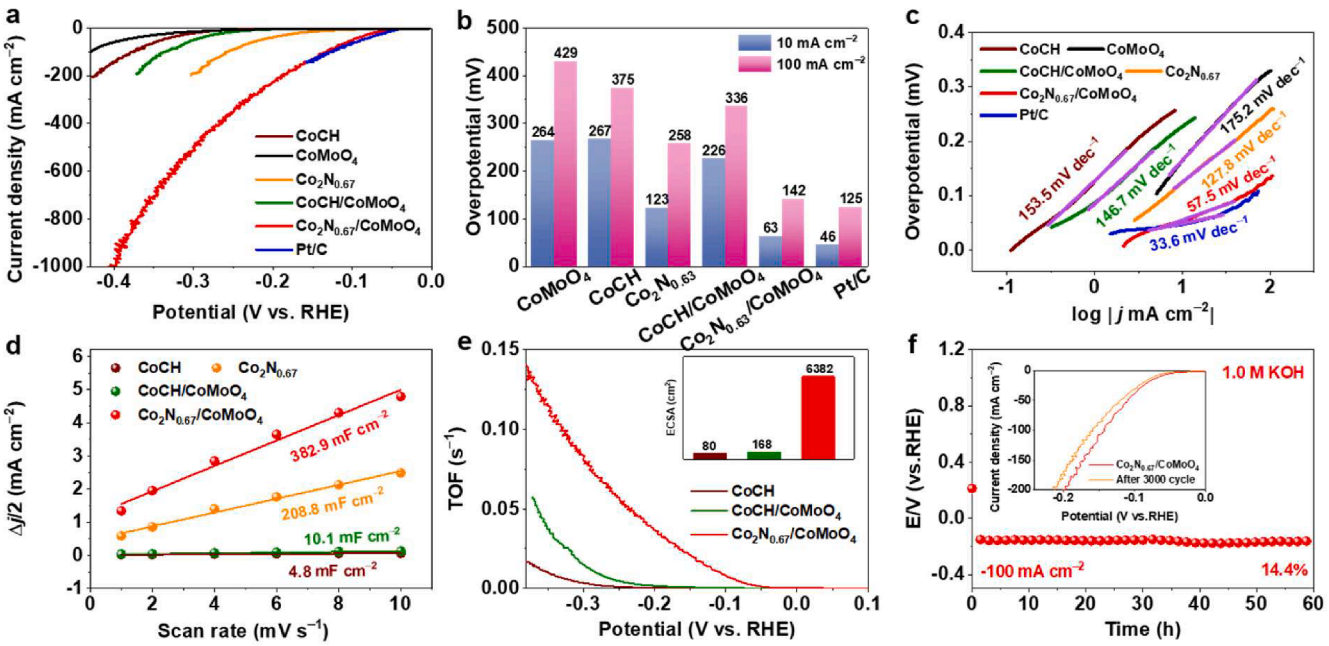

Fig. 3. Electrocatalytic HER performance. (a) LSV polarization curves, (b) the comparison of overpotential at 10 and 100 mA cm^{-2} for $Co_2N_{0.67}$/$CoMoO_4$ and other references, (c) corresponding Tafel slopes, (d) summarized double-layer capacitance (C_{dl}) of different catalysts in 1.0 M KOH. (e) Potential-dependent TOF curves (Inset: a bar chart of the ECSA) of CoCH, CoCH/$CoMoO_4$, and $Co_2N_{0.67}$/$CoMoO_4$, respectively. (f) Durability tests of $Co_2N_{0.67}$/$CoMoO_4$ for HER at −100 mA cm^{-2} and (Inset: Polarization curve before and after 3000 cycles of cyclic voltammetric stability test in 1.0 M KOH solution).

$CoMoO_4$ has the best HER activity when the adding amount of Na_2MoO_4 is 150 mg mL^{-1} (Fig. S9). The study indicates that the HER performance is related to the available interface between $Co_2N_{0.67}$ and $CoMoO_4$. The best HER performance was achieved when the $NaMoO_4$ used is 0.15 g, and the ratio of the two components is close to 1:1, which may lead to the most accessible interface (Table S1) [18]. To further explore the influencing factors of catalytic kinetics, the electrochemical double-layer capacitance (C_{dl}) was measured by cyclic voltammetry (CV) measurements in the non-Faradaic region at different scan rates (Fig. S10). In Fig. 3d, the C_{dl} of $Co_2N_{0.67}$/$CoMoO_4$ is 382.9 mF cm^{-2}, larger than those of CoCH (4.8 mF cm^{-2}), $Co_2N_{0.67}$ (208.8 mF cm^{-2}), and CoCH/$CoMoO_4$ (10.1 mF cm^{-2}). Generally, electrochemically active surface area (ECSA) is directly proportional to C_{dl}, and is used to estimate the number of active sites. To be specific, the $Co_2N_{0.67}$/$CoMoO_4$ retains the maximum ECSA of 6382 cm^2, which surpasses CoCH (80 cm^2), CoCH/$CoMoO_4$ (168 cm^2), $Co_2N_{0.67}$/$CoMoO_4$-100 (3553 cm^2), and $Co_2N_{0.67}$/$CoMoO_4$-200 (5106 cm^2), suggesting that the $Co_2N_{0.67}$/$CoMoO_4$ catalyst has more active sites (inset: Fig. 3e and Fig. S11). The more active sites may be caused by the generation of oxygen vacancies and the formation of the abundant interface on rough nanosheets after nitriding treatment, which can increase the contact area between the catalyst and the electrolyte to provide more active sites for HER point [53]. Notably, the LSV polarization curves are normalized by ECSA indicating that $Co_2N_{0.67}$/$CoMoO_4$ has the lowest overpotential (Fig. S12) [54,55]. This result confirms that the strong interfacial interaction between $Co_2N_{0.67}$ and $CoMoO_4$ species increases ECSA and enhances intrinsic activity. The turn over frequency (TOF) value of $Co_2N_{0.67}$/$CoMoO_4$ greatly increased compared with CoCH and CoCH/$CoMoO_4$, similarly meaning that the $Co_2N_{0.67}$/$CoMoO_4$ catalyst increased intrinsic activity after nitriding treatment, thus improving the catalytic activity (Fig. 3e) [53]. Considering the high performance of $Co_2N_{0.67}$/$CoMoO_4$, we carried out a long-term stability test at a constant current density of −100 mA cm^{-2}, and the results showed that the current density has declined by approximately 14.4% after 60 h (Fig. 3f). In addition, the stability of the catalyst was further explored through multi-cycle CV testing (inset: Fig. 3f) and the polarization curve dropped slightly after 3000 cycles. The degradation of catalytic performance can be attributed to part of the morphology agglomeration (Fig. S13), slight changes in crystal structure (Fig. S14) and chemical valence (Fig. S15), as well as the combined effect of the dissolution of $CoMoO_4$ [56,57].

3.4. Electrocatalytic OER analysis

The OER catalytic performance was also evaluated by linear sweep voltammetry (LSV) polarization in 1.0 M KOH. As shown in Fig. 4a, the overpotential required for $Co_2N_{0.67}$/$CoMoO_4$ catalyst is 283 mV at a current density of 10 mA cm^{-2}, which is slightly higher than that of commercial RuO_2, but far less than those of other comparative OER catalysts (Table S3). Remarkably, the performance of $Co_2N_{0.67}$/$CoMoO_4$ is superior to RuO_2 at a high current density (>40 mA cm^{-2}) due to a mesoporous nanosheet structure that has better conductivity and small bubble size [58,59]. Tafel slopes are shown in Fig. 4b, the $Co_2N_{0.67}$/$CoMoO_4$ shows a smaller Tafel slope among all other OER catalysts, suggesting faster reaction kinetics in the OER process, which can be attributed to the synergistic effect between $Co_2N_{0.67}$ and $CoMoO_4$ [4,60]. Besides, the $Co_2N_{0.67}$/$CoMoO_4$ has a smaller R_{ct} value than CoCH, $CoMoO_4$, $Co_2N_{0.67}$, and CoCH/$CoMoO_4$, revealing a faster charge transfer than others (Fig. 4c). Notably, the microscopic morphology changes little after stability (Fig. S16). The XRD and XPS analysis indicated that the chemical valences of the elements have not changed evidently after the stability test (Fig. S15 and Fig. S17), and Energy dispersive spectroscopy (EDS) shows that only 0.1% of Mo species remained on the surface (Fig. S18), which may be caused by the dissolution of Mo species during the OER process [61].

3.5. DFT calculations

Using density functional theory (DFT) calculations to further understand the excellent HER and OER activity. The differential charge density of the heterojunction shows that there is obvious charge accumulation at the interface of the two materials, indicating that $Co_2N_{0.67}$ and $CoMoO_4$ have strong interaction and synergistic effects (Fig. 5a). To further elucidate the interaction between $Co_2N_{0.67}$ and $CoMoO_4$ in heterojunction catalysts, the density of states (DOS) of $Co_2N_{0.67}$,

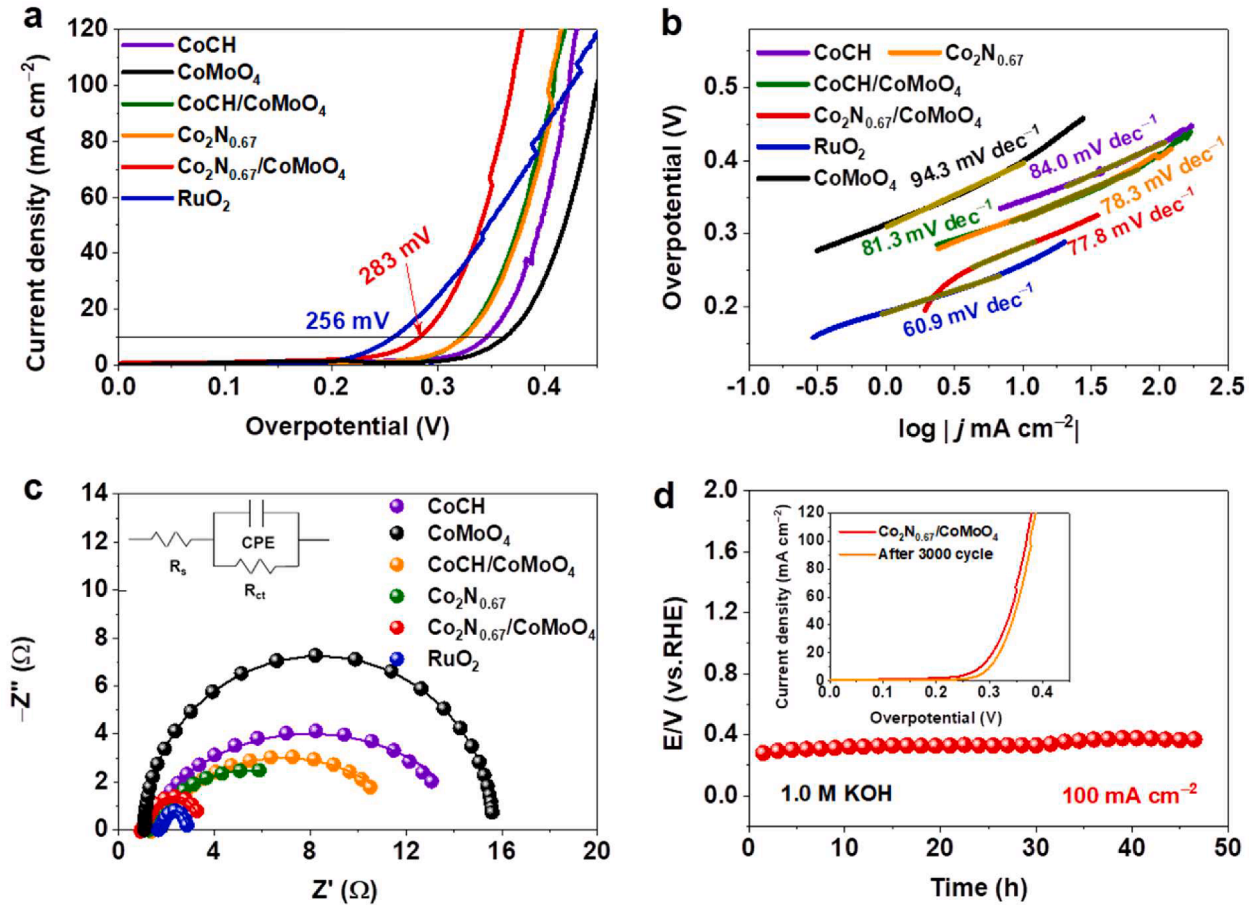

Fig. 4. Electrocatalytic OER performance in 1.0 M KOH. (a) LSV polarization curves, and (b) the corresponding Tafel slopes of different catalysts. (c) Electrochemical impedance spectroscopy (EIS) of different catalysts. (d) Durability tests of $Co_2N_{0.67}$/$CoMoO_4$ for HER at 100 mA cm^{-2} and (Inset: Polarization curve before and after 3000 cycles of cyclic voltammetric stability test in 1.0 M KOH solution).

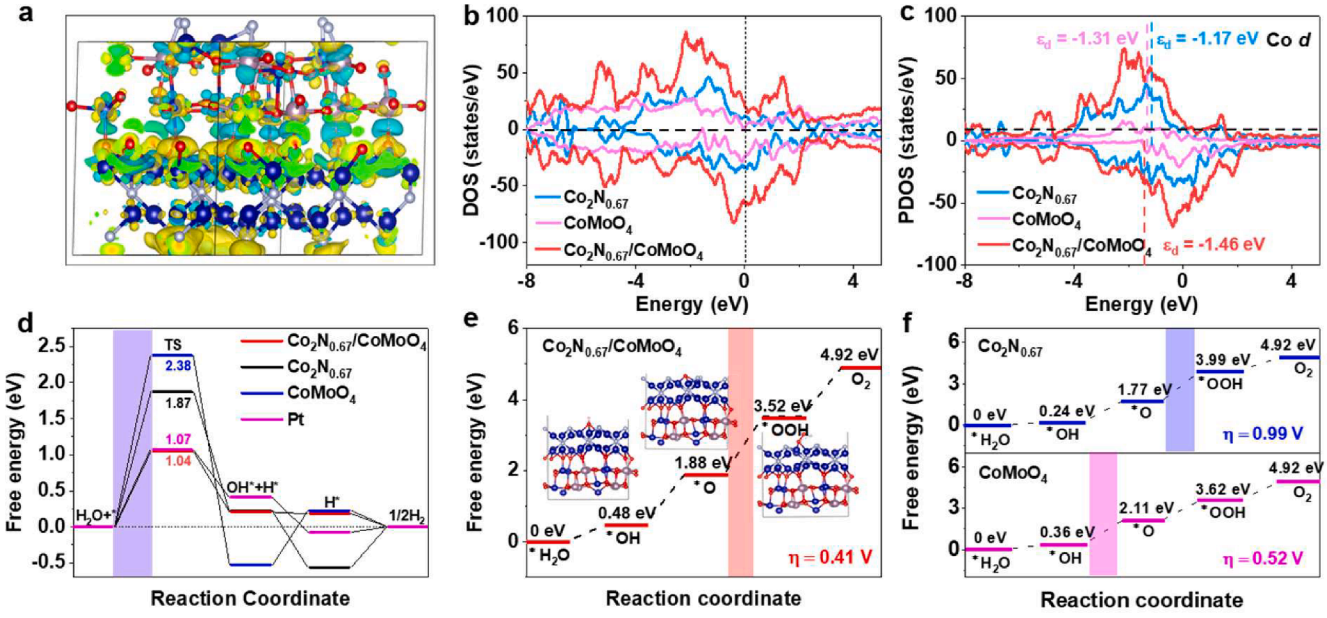

Fig. 5. Density functional theory (DFT) calculations on $Co_2N_{0.67}$, $CoMoO_4$ and $Co_2N_{0.67}$/$CoMoO_4$. (a) Schematic diagram of differential charge structure model. The blue, pink, red, and silver balls represent the Co, Mo, O, and N atoms, respectively. (b) The density of states (DOS) of $Co_2N_{0.67}$, $CoMoO_4$, and $Co_2N_{0.67}$/$CoMoO_4$. (c) Projection DOS (PDOS) of Co 3*d* track of $Co_2N_{0.67}$, $CoMoO_4$, and $Co_2N_{0.67}$/$CoMoO_4$. The dotted line represents the center of the d-band of the catalyst. (d) Free energy diagram of H adsorption (ΔG_{H^*}) for $Co_2N_{0.67}$, $CoMoO_4$, and $Co_2N_{0.67}$/$CoMoO_4$. (e,f) Free-energy diagrams of $Co_2N_{0.67}$, $CoMoO_4$, and $Co_2N_{0.67}$/$CoMoO_4$ for OER.

$CoMoO_4$, and $Co_2N_{0.67}/CoMoO_4$ structures were calculated. As shown from Fig. S19, Co atom in $Co_2N_{0.67}$ shows a higher electron density near the E_F and more positive E_d, which can infer this Co species act as main active sites [62]. The Co atom in $CoMoO_4$ serves as a backup electron reservoir to transfer the electron of Mo species and protect the valence of the Co of $Co_2N_{0.67}$ [63]. It is note that the *d-d* coupling between two Co species enabled the higher electron density of $Co_2N_{0.67}/CoMoO_4$ near the Fermi level, which can accelerate the electron transfer on the surface to improve the performances of water splitting (Fig. 5b) [64]. In addition, the *d*-band center position of the Co atom in the $Co_2N_{0.67}/CoMoO_4$ structure is moved down to −1.46 eV compared with the single $Co_2N_{0.67}$ (ε_d = -1.17 eV) and $CoMoO_4$ (ε_d = -1.31 eV) which led to more optimal H_{ads} and thereby pronouncedly be conducive to following reactions (Fig. 5c) [65].

The intrinsic catalytic activity during the alkaline HER process was further investigated by Gibbs free energy of Pt, $Co_2N_{0.67}$, $CoMoO_4$, and $Co_2N_{0.67}/CoMoO_4$ (Fig. 5d). Generally, the activation of the H_2O molecule for the transition state (TS) is the rate-determining step for alkaline HER [66,67]. Obviously, $Co_2N_{0.67}/CoMoO_4$ heterostructure demonstrates a desired activation energy barrier of 1.04 eV lower than Pt (1.07 eV), $Co_2N_{0.67}$ (1.87 eV), and $CoMoO_4$ (2.38 eV), implying the combination of $Co_2N_{0.67}$ and $CoMoO_4$ can remarkably accelerate the disintegration of H_2O to achieve a faster HER kinetics. A desirable HER catalyst should demonstrate a moderate hydrogen binding energy (HBE) in the Heyrovsky step to adjust the adsorption of H* and the following desorption of H_2 [68,69]. The $Co_2N_{0.67}/CoMoO_4$ heterostructure shows a more suitable HBE value of 0.18 eV comparing the $Co_2N_{0.67}$ and $CoMoO_4$ of − 0.56 and 0.23 eV, implying the $Co_2N_{0.67}/CoMoO_4$ heterostructure is more efficient to the production of H_2 and the corresponding schematic *H adsorption models are shown in Figs. S20-S21. In this light, synergistic effects between the $Co_2N_{0.67}$ and $CoMoO_4$ promote HER performance through accelerating the kinetics of HER by lowering the energy barrier for water dissociation and regulating the HBE. Also, we calculated the free energy distribution of OER to explore the OER mechanism. The OER process involves multiple steps in alkaline solutions, including *OH, *O, *OOH, and O_2 intermediates (Fig. 5e, f and Fig. S22) [27,70]. Since the Mo active site in $CoMoO_4$ is unstable during the adsorption process, only the free energy diagrams of the Co-active site in different catalysts are shown here. As shown in Fig. 5e, for $Co_2N_{0.67}/CoMoO_4$, the electron transfer step from *O to *OOH (Step III) has the highest free energy gradient, indicating that it is the rate-determining step of the OER process with a theoretical overpotential of 0.17 eV. The theoretical overpotential of $Co_2N_{0.67}$ and $CoMoO_4$ was 0.2 V and 0.47 V, respectively, both higher than 0.17 eV (Fig. 5f). The DFT study indicated that $Co_2N_{0.67}/CoMoO_4$ heterostructure composite has better OER catalytic activity. Notably, the trends of HER and OER activity in the theoretical calculations are consistent with our experimental results, which confirm that interfacial synergy is a viable mechanism for producing the high-performance electrocatalysts for overall water splitting.

3.6. Overall water splitting and Zn-H_2O cell analysis

In the light of the bifunctional HER and OER nature, we fabricated a

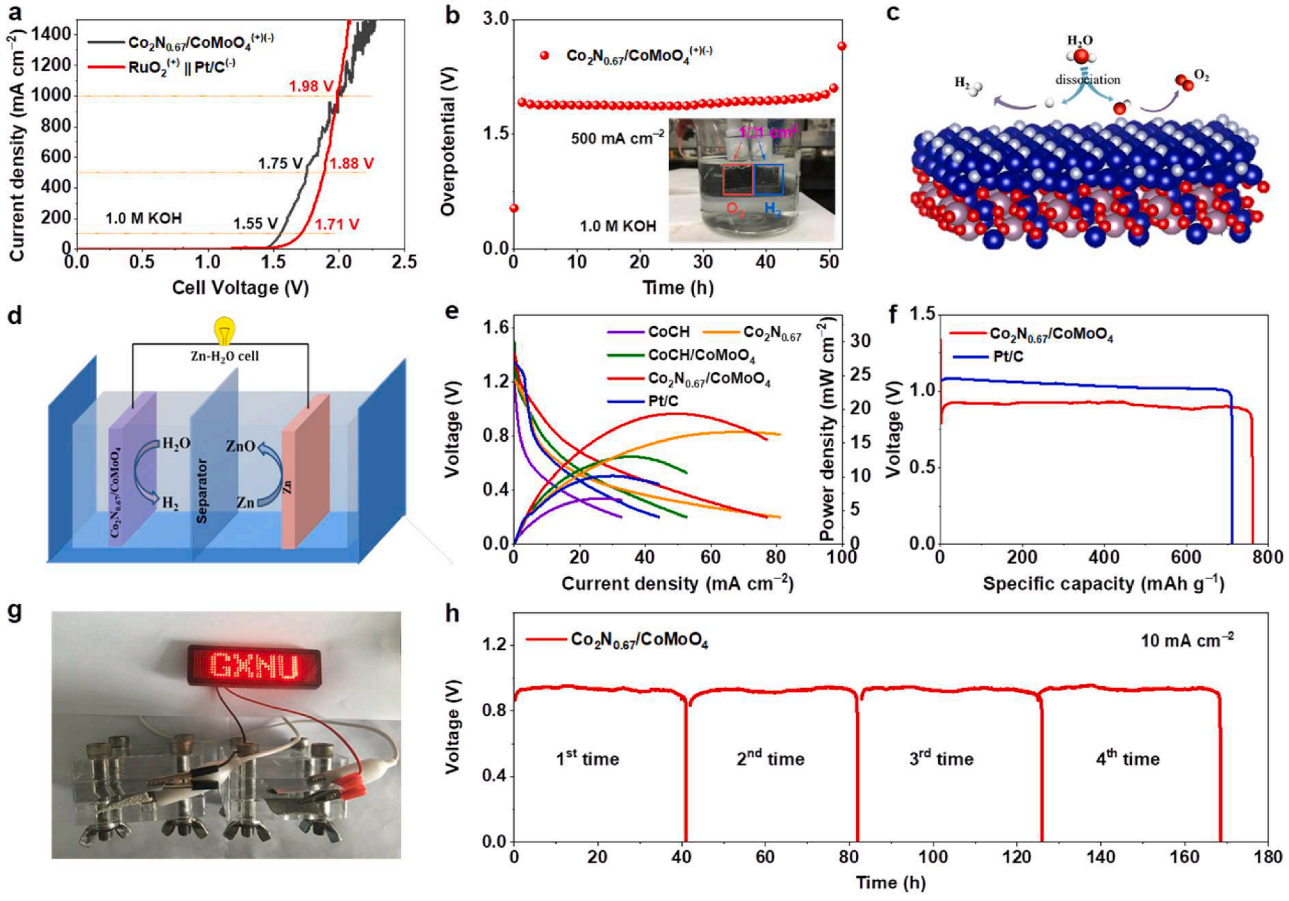

Fig. 6. (a) Polarization curves of the bifunctional $Co_2N_{0.67}/CoMoO_4^{(+/-)}$ and $RuO_2^{(+)}||Pt/C^{(-)}$ catalysts for overall water splitting. (b) Chronopotentiometry curve of the bifunctional $Co_2N_{0.67}/CoMoO_4^{(+/-)}$ at a current density of 500 mA cm^{-2} in 1.0 M KOH. (c) Schematic illustration of the prepared $Co_2N_{0.67}/CoMoO_4$ for HER and OER. (d) The graphical illustration of the homemade Zn-H_2O cell. (e) Polarization curves and corresponding power density plots of CoCH, Pt/C, and other catalysts. (f) The galvanostatic discharge curve at 10 mA cm^{-2} of $Co_2N_{0.67}/CoMoO_4$ and Pt/C. (g) A photograph of LED screen light powered by two series-connected $Co_2N_{0.67}/CoMoO_4$ based Zn-H_2O cells in series. (h) Long-term durability tests for Zn-H_2O cells using $Co_2N_{0.67}/CoMoO_4$ as the cathode.

total water splitting system using $Co_2N_{0.67}/CoMoO_4$ as anode and cathode in a two-electrode system in 1.0 M KOH, respectively. In Fig. 6a, the $Co_2N_{0.67}/CoMoO_4^{(+/-)}$ system requires relatively low cell voltages of 1.71, 1.88, and 1.98 V to afford the current densities of 100, 500, and 1000 mA cm^{-2} (Table S4). In particular, the $Co_2N_{0.67}/CoMoO_4^{(+/-)}$ outperformed $RuO_2^{(+)}||Pt/C^{(-)}$ two-electrode system at 1000 mA cm^{-2} current density. Excitingly, $Co_2N_{0.67}/CoMoO_4^{(+/-)}$ displays the outstanding stability for 50 h at a high current density of 500 mA cm^{-2} (Fig. 6b). However, the stability decreased mildly after 50 h, which may be related to the structural damage of the hybrid material (Fig. S23). The excellent electrocatalytic activity is attributed to the interface promoted H_2O dissociation and the desorption of reaction intermediates on the Co-active site (Fig. 6c).

Fig. 6d shows a simple assembly diagram of the cell, in which the Zn plate as anode, $Co_2N_{0.67}/CoMoO_4$ catalyst as cathode, and 6 M KOH and 0.2 M $Zn(Ac)_2$ as an electrolyte, to further study the feasibility of $Co_2N_{0.67}/CoMoO_4$ in Zn-H_2O cell [71,72]. In Fig. 6e, $Co_2N_{0.67}/CoMoO_4$ has the highest peak-power density of 20 mW cm^{-2} among the other comparative catalysts. Noticeably, the cell with $Co_2N_{0.67}/CoMoO_4$ showed a specific capacity of 750 mAh g^{-1} at the discharge current density of 10 mA cm^{-2}, which is higher than that of Pt/C based Zn-H_2O cell (700 mAh g^{-1}) (Fig. 6f). Additionally, galvanostatic discharge–charge curves were investigated at a current density of 5 mA cm^{-2} for 100 h. The $Co_2N_{0.67}/CoMoO_4$-based Zn-H_2O cell displayed excellent stability and reversibility (Fig. S24). More remarkably, two rechargeable Zn-H_2O cell in series can continuously light a LED screen light, also proves the potential application of the $Co_2N_{0.67}/CoMoO_4$-based cell (Fig. 6g). The Zn-H_2O cell was deactivated after 41 h because the generated ZnO fully covered the Zn plate (anode) (Fig. 6h and Fig. S25). We then resurrected the cell by replacing a new electrolyte and zinc plate and cleaning the $Co_2N_{0.67}/CoMoO_4$ with 0.5 M H_2SO_4. The Zn-H_2O cell showed strong discharge stability of nearly 170 h after four resurrections at a current density of 10 mA cm^{-2}. The catalyst morphology has not changed significantly (Fig. S26), demonstrating its potential for industrial applications.

4. Conclusion

In summary, a heterogeneous catalyst with interfacial structure was synthesized by hydrothermal method and ammonia etching for overall water splitting and Zn-H_2O cell. The results showed that the $Co_2N_{0.67}/CoMoO_4$ catalyst exhibited excellent catalytic activity and high stability in both HER, OER, overall-water splitting as well as Zn-H_2O cells. The DFT calculations suggest that the self-supporting open structure of the CC in $Co_2N_{0.67}/CoMoO_4$ and the interface between $Co_2N_{0.67}$ and $CoMoO_4$ can enable the catalyst to expose more active sites thereby improving the intrinsic activity through adjusting the binding energy of the intermediates. As a result, the optimized catalyst exhibited outstanding catalytic performance better than most existing non-precious metal catalysts. This work provides an attractive interface engineering strategy for the rational design of non-noble metal electrocatalysts for clean energy conversion.

Declaration of Competing Interest

The authors declare that they have no known competing financial interests or personal relationships that could have appeared to influence the work reported in this paper.

Acknowledgements

This work has been supported by the National Natural Science Foundation of China (no. 21965005), Natural Science Foundation of Guangxi Province (2018GXNSFAA294077, 2021GXNSFAA076001), Project of High-Level Talents of Guangxi (F-KA18015), and Guangxi Technology Base and Talent Subject (GUIKE AD18126001, GUIKE AD20297039).

Appendix A. Supplementary data

Supplementary data to this article can be found online at https://doi.org/10.1016/j.cej.2022.134795.

References

[1] K. Zhu, J. Chen, W. Wang, J. Liao, J. Dong, M.O.L. Chee, N. Wang, P. Dong, P. M. Ajayan, S. Gao, J. Shen, M. Ye, Etching-doping sedimentation equilibrium strategy: accelerating kinetics on hollow Rh-Doped CoFe-layered double hydroxides for water splitting, Adv. Funct. Mater. 30 (35) (2020) 2003556.
[2] Q. Qian, J. Zhang, J. Li, Y. Li, X.u. Jin, Y. Zhu, Y.i. Liu, Z. Li, A. El-Harairy, C. Xiao, G. Zhang, Y.i. Xie, Artificial heterointerfaces achieve delicate reaction kinetics towards hydrogen evolution and hydrazine oxidation catalysis, Angew. Chem. Int. Ed. 60 (11) (2021) 5984–5993.
[3] G. Qian, J. Chen, T. Yu, L. Luo, S. Yin, N-doped graphene-decorated NiCo alloy coupled with mesoporous NiCoMoO nano-sheet heterojunction for enhanced water electrolysis activity at high current density, Nano-Micro Lett. 13 (2021) 77.
[4] Z. Liu, D. Liu, L. Zhao, J. Tian, J. Yang, L. Feng, Efficient overall water splitting catalyzed by robust $FeNi_3N$ nanoparticles with hollow interiors, J. Mater. Chem. A 9 (12) (2021) 7750–7758.
[5] Y. Lu, Z. Li, Y. Xu, L. Tang, S. Xu, D.i. Li, J. Zhu, D. Jiang, Bimetallic Co-Mo nitride nanosheet arrays as high-performance bifunctional electrocatalysts for overall water splitting, Chem. Eng. J. 411 (2021) 128433.
[6] Y. Duan, J.Y. Lee, S. Xi, Y. Sun, J. Ge, S.J.H. Ong, Y. Chen, S. Dou, F. Meng, C. Diao, A. Fisher, G.G. Scherer, X. Wang, A. Grimaud, Z. Xu, Anodic oxidation enabled cation leaching for promoting surface reconstruction in water oxidation, Angew. Chem. Int. Ed. 60 (2021) 7418–7425.
[7] L. Bai, S. Lee, X. Hu, Spectroscopic and Electrokinetic Evidence for a Bifunctional Mechanism of the Oxygen Evolution Reaction, Angew. Chem. Int. Ed. 60 (2021) 3095–3103.
[8] N. Yu, W. Cao, M. Huttula, Y. Kayser, P. Hoenicke, B. Beckhoff, F. Lai, R. Dong, H. Sun, B. Geng, Fabrication of FeNi hydroxides double-shell nanotube arrays with enhanced performance for oxygen evolution reaction, Appl. Catal. B: Environ. 261 (2020), 118193.
[9] S. Choi, J. Park, M.K. Kabiraz, Y. Hong, T. Kwon, T. Kim, A. Oh, H. Baik, M. Lee, S. M. Paek, S.I. Choi, K. Lee, Pt dopant: controlling the Ir oxidation states toward efficient and durable oxygen evolution reaction in acidic media, Adv. Funct. Mater. 30 (2020) 2003935.
[10] Y. Zhao, H. Cong, P. Li, D. Wu, S. Chen, W. Luo, Hexagonal $RuSe_2$ Nanosheets for Highly Efficient Hydrogen Evolution Electrocatalysis, Angew. Chem. Int. Ed. 60 (2021) 7013–7017.
[11] Z. Wang, B. Xiao, Z. Lin, Y. Xu, Y. Lin, F. Meng, Q. Zhang, L. Gu, B. Fang, S. Guo, W. Zhong, $PtSe_2$/Pt heterointerface with reduced coordination for boosted hydrogen evolution reaction, Angew. Chem. Int. Ed. 60 (43) (2021) 23388–23393.
[12] D. Chen, T. Liu, P. Wang, J. Zhao, C. Zhang, R. Cheng, W. Li, P. Ji, Z. Pu, S. Mu, Ionothermal route to phase-pure RuB_2 catalysts for efficient oxygen evolution and water splitting in acidic media, ACS Energy Lett. 5 (9) (2020) 2909–2915.
[13] J. Liu, G. Qian, H. Zhang, J. Chen, Y. Wang, H. He, L. Luo, S. Yin, Amorphous FeOOH coating stabilizes WO_2-Na_xWO_3 for accelerating oxygen evolution reaction, Chem. Eng. J. 426 (2021) 131253.
[14] L. Kuai, E. Kan, W. Cao, M. Huttula, S. Ollikkala, T. Ahopelto, A.-P. Honkanen, S. Huotari, W. Wang, B. Geng, Mesoporous $LaMnO_{3+\delta}$ perovskite from spray−pyrolysis with superior performance for oxygen reduction reaction and Zn−air battery, Nano Energy 43 (2018) 81–90.
[15] D.C. Nguyen, T.L. Luyen Doan, S. Prabhakaran, D.T. Tran, D.H. Kim, J.H. Lee, N. H. Kim, Hierarchical Co and Nb dual-doped MoS_2 nanosheets shelled micro-TiO_2 hollow spheres as effective multifunctional electrocatalysts for HER, OER, and ORR, Nano Energy 82 (2021) 105750.
[16] A. Wu, Y. Gu, Y. Xie, H. Yan, Y. Jiao, D. Wang, C. Tian, Interfacial engineering of MoS_2/MoN heterostructures as efficient electrocatalyst for pH-universal hydrogen evolution reaction, J. Alloy. Compd. 867 (2021), 159066.
[17] T. Zhao, X. Shen, Y. Wang, R.K. Hocking, Y. Li, C. Rong, K. Dastafkan, Z. Su, C. Zhao, In situ reconstruction of V-doped Ni_2P Pre-catalysts with tunable electronic structures for water oxidation, Adv. Funct. Mater. 31 (2021) 2100614.
[18] X. Huang, X. Xu, X. Luan, D. Cheng, CoP nanowires coupled with CoMoP nanosheets as a highly efficient cooperative catalyst for hydrogen evolution reaction, Nano Energy 68 (2020), 104332.
[19] N. Yao, R. Meng, J. Su, Z. Fan, P. Zhao, W. Luo, Dual-phase engineering of MoN/Co_4N with tailored electronic structure for enhanced hydrogen evolution, Chem. Eng. J. 421 (2021), 127757.
[20] J. Sun, W. Xu, C. Lv, L. Zhang, M. Shakouri, Y. Peng, Q. Wang, X. Yang, D. Yuan, M. Huang, Y. Hu, D. Yang, L. Zhang, Co/MoN hetero-interface nanoflake array with enhanced water dissociation capability achieves the Pt-like hydrogen evolution catalytic performance, Appl. Catal. B: Environ. 286 (2021), 119882.
[21] B.o. Geng, F. Yan, L. Liu, C. Zhu, B. Li, Y. Chen, Ni/MoC heteronanoparticles encapsulated within nitrogen-doped carbon nanotube arrays as highly efficient self-supported electrodes for overall water splitting, Chem. Eng. J. 406 (2021) 126815.

[22] C. Zhu, Z. Yin, W. Lai, Y. Sun, L. Liu, X. Zhang, Y. Chen, S.-L. Chou, Fe-Ni-Mo nitride porous nanotubes for full water splitting and Zn-air batteries, Adv. Energy Mater. 8 (36) (2018) 1802327.
[23] F. Ma, S. Wang, X. Liang, C. Wang, F. Tong, Z. Wang, P. Wang, Y. Liu, Y. Dai, Z. Zheng, B. Huang, Ni_3B as a highly efficient and selective catalyst for the electrosynthesis of hydrogen peroxide, Appl. Catal. B: Environ. 279 (2020) 119371.
[24] X. Ma, K. Li, X. Zhang, B.o. Wei, H. Yang, L. Liu, M. Zhang, X. Zhang, Y. Chen, The surface engineering of cobalt carbide spheres through N, B co-doping achieved by room-temperature in situ anchoring effects for active and durable multifunctional electrocatalysts, J. Mater. Chem. A 7 (24) (2019) 14904–14915.
[25] Z. Li, Y.i. Feng, Y.-L. Liang, C.-Q. Cheng, C.-K. Dong, H. Liu, X.-W. Du, Stable rhodium (IV) oxide for alkaline hydrogen evolution reaction, Adv. Mater. 32 (25) (2020) 1908521.
[26] W. Hu, Q. Shi, Z. Chen, H. Yin, H. Zhong, P. Wang, $Co_2N/Co_2Mo_3O_8$ heterostructure as a highly active electrocatalyst for an alkaline hydrogen evolution reaction, ACS Appl. Mater. Interfaces 13 (2021) 8337–8343.
[27] W. Yuan, S. Wang, Y. Ma, Y. Qiu, Y. An, L. Cheng, Interfacial engineering of cobalt nitrides and mesoporous nitrogen-doped carbon: toward efficient overall water-splitting activity with enhanced charge-transfer efficiency, ACS Energy Lett. 5 (2020) 692–700.
[28] P. Zhou, G.Y. Zhai, X.S. Lv, Y.Y. Liu, Z.Y. Wang, P. Wang, Z.K. Zheng, H.F. Cheng, Y. Dai, B.B. Huang, Boosting the electrocatalytic HER performance of Ni_3N-V_2O_3 via the interface coupling effect, Appl. Catal. B: Environ. 283 (2021), 119590.
[29] X. Zheng, X. Han, Y. Cao, Y. Zhang, D. Nordlund, J. Wang, S. Chou, H. Liu, L. Li, C. Zhong, Y. Deng, W. Hu, Identifying dense $NiSe_2/CoSe_2$ heterointerfaces coupled with surface high-valence bimetallic sites for synergistically enhanced oxygen electrocatalysis, Adv. Mater. 32 (2020) 2000607.
[30] R.-Q. Li, X.-Y. Wan, B.-L. Chen, R.-Y. Cao, Q.-H. Ji, J. Deng, K.-G. Qu, X.-B. Wang, Y.-C. Zhu, Hierarchical $Ni_3N/Ni_{0.2}Mo_{0.8}N$ heterostructure nanorods arrays as efficient electrocatalysts for overall water and urea electrolysis, Chem. Eng. J. 409 (2021), 128240.
[31] W. Liu, L. Yu, R. Yin, X. Xu, J. Feng, X. Jiang, D. Zheng, X. Gao, X. Gao, W. Que, P. Ruan, F. Wu, W. Shi, X. Cao, Non-3d metal modulation of a 2D Ni-Co heterostructure array as multifunctional electrocatalyst for portable overall water splitting, Small 16 (2020) 1906775.
[32] B.C.M. Martindale, E. Reisner, Bi-functional iron-only electrodes for efficient water splitting with enhanced stability through in situ electrochemical regeneration, Adv. Energy Mater. 6 (2016) 1502095.
[33] M.W. Kanan, D.G. Nocera, In situ formation of an oxygen-evolving catalyst in neutral water containing phosphate and Co^{2+}, Science 321 (2008) 1072–1075.
[34] N. Kornienko, N. Heidary, G. Cibin, E. Reisner, Catalysis by design: development of a bifunctional water splitting catalyst through an operando measurement directed optimization cycle, Chem. Sci. 9 (2018) 5322–5333.
[35] D. Guo, Z. Wan, Y. Li, B. Xi, C. Wang, $TiN@Co_{5.47}N$ composite material constructed by atomic layer deposition as reliable electrocatalyst for oxygen evolution reaction, Adv. Funct. Mater. 31 (2020) 2008511.
[36] N.a. Yao, R. Meng, F. Wu, Z. Fan, G. Cheng, W. Luo, Oxygen-vacancy-induced CeO_2/Co_4N heterostructures toward enhanced pH-Universal hydrogen evolution reactions, Appl. Catal. B: Environ. 277 (2020) 119282.
[37] T. Yu, Q. Xu, L. Luo, C. Liu, S. Yin, Interface engineering of NiO/RuO_2 heterojunction nano-sheets for robust overall water splitting at large current density, Chem. Eng. J. 430 (2022) 133117.
[38] P. Cai, Y. Li, G. Wang, Z. Wen, Alkaline-Acid Zn-H_2O Fuel Cell for the Simultaneous Generation of Hydrogen and Electricity, Angew. Chem. Int. Ed. 57 (15) (2018) 3910–3915.
[39] H. He, H. Qin, J. Wu, X. Chen, R. Huang, F. Shen, Z. Wu, G. Chen, S. Yin, J. Liu, Engineering interfacial layers to enable Zn metal anodes for aqueous zinc-ion batteries, Energy Storage Mater. 43 (2021) 317–336.
[40] T. Liu, M. Li, Z. Su, X. Bo, W. Guan, M. Zhou, Monodisperse and Tiny $Co_2N_{0.67}$ nanocrystals uniformly embedded over two curving surfaces of hollow carbon microfibers as efficient electrocatalyst for oxygen evolution reaction, ACS Appl. Nano Mater. 1 (9) (2018) 4461–4473.
[41] X. Zhang, F. Zhou, W. Pan, Y. Liang, R. Wang, General construction of molybdenum-based nanowire arrays for pH-universal hydrogen evolution electrocatalysis, Adv. Funct. Mater. 28 (2018) 1804600.
[42] Y.u. Liu, Y. Xing, S. Xu, Y. Lu, S. Sun, D. Jiang, Interfacing Co_3Mo with $CoMoO_x$ for synergistically boosting electrocatalytic hydrogen and oxygen evolution reactions, Chem. Eng. J. 431 (2022) 133240.
[43] L. Zhao, Z. Yang, Q. Cao, L. Yang, X. Zhang, J. Jia, Y. Sang, H.-J. Wu, W. Zhou, H. Liu, An earth-abundant and multifunctional Ni nanosheets array as electrocatalysts and heat absorption layer integrated thermoelectric device for overall water splitting, Nano Energy 56 (2019) 563–570.
[44] K. Song, W. Li, J. Xin, Y. Zheng, X. Chen, R. Yang, W. Lv, Q. Li, Hierarchical porous heterostructured $Co(OH)_2/CoSe_2$ nanoarray: A controllable design electrode for advanced asymmetrical supercapacitors, Chem. Eng. J. 419 (2021), 129435.
[45] J. Diao, Y. Qiu, S. Liu, W. Wang, K. Chen, H. Li, W. Yuan, Y. Qu, X. Guo, Interfacial engineering of W_2N/WC heterostructures derived from solid-state synthesis: A Highly efficient trifunctional electrocatalyst for ORR, OER, and HER, Adv. Mater. 32 (2020), e1905679.
[46] Y. Hu, H. Yu, L. Qi, J. Dong, P. Yan, T. Taylor Isimjan, X. Yang, Interface engineering of needle-like P-doped MoS_2/CoP arrays as highly active and durable bifunctional electrocatalyst for overall water splitting, ChemSusChem 14 (2021) 1565–1573.
[47] M. Guo, M. Xu, Y. Qu, C. Hu, P. Yan, T.T. Isimjan, X. Yang, Electronic/mass transport increased hollow porous Cu_3P/MoP nanospheres with strong electronic interaction for promoting oxygen reduction in Zn-air batteries, Appl. Catal. B: Environ. 297 (2021), 120415.
[48] F. Lin, Z. Dong, Y. Yao, L. Yang, F. Fang, L. Jiao, Electrocatalytic hydrogen evolution of ultrathin Co-Mo_5N_6 heterojunction with interfacial electron redistribution, Adv. Energy Mater. 10 (2020) 2002176.
[49] J. He, W. Li, P. Xu, J. Sun, Tuning electron correlations of RuO_2 by co-doping of Mo and Ce for boosting electrocatalytic water oxidation in acidic media, Appl. Catal. B: Environ. 298 (2021), 120528.
[50] P. Zhou, X. Lv, D. Xing, F. Ma, Y. Liu, Z. Wang, P. Wang, Z. Zheng, Y. Dai, B. Huang, High-efficient electrocatalytic overall water splitting over vanadium doped hexagonal $Ni_{0.2}Mo_{0.8}N$, Appl. Catal. B: Environ. 263 (2020), 118330.
[51] S. Dou, W. Zhang, Y. Yang, S. Zhou, X. Rao, P. Yan, T.T. Isimjan, X. Yang, Shaggy-like Ru-clusters decorated core-shell metal-organic framework-derived CoO_x@NPC as high-efficiency catalyst for $NaBH_4$ hydrolysis, Int. J. Hydrogen Energy 46 (2021) 7772–7781.
[52] M. Zhao, W. Li, J. Li, W. Hu, C.M. Li, Strong electronic interaction enhanced electrocatalysis of metal sulfide clusters embedded metal-organic framework ultrathin nanosheets toward highly efficient overall water splitting, Adv. Sci. 7 (2020) 2001965.
[53] S.L. Zhang, B.Y. Guan, X.F. Lu, S. Xi, Y. Du, X.W.D. Lou, Metal atom-doped Co_3O_4 hierarchical nanoplates for electrocatalytic oxygen evolution, Adv. Mater. 32 (2020) 2002235.
[54] T.X. Nguyen, Y.C. Liao, C.C. Lin, Y.H. Su, J.M. Ting, Advanced high entropy perovskite oxide electrocatalyst for oxygen evolution reaction, Adv. Funct. Mater. 31 (2021) 2101632.
[55] B. Geng, F. Yan, X. Zhang, Y. He, C. Zhu, S.L. Chou, X. Zhang, Y. Chen, Conductive CuCo-based bimetal organic framework for efficient hydrogen evolution, Adv. Mater. 33 (2021) 2106781.
[56] J. Zhang, L. Zhang, L.i. Du, H.L. Xin, J.B. Goodenough, Z. Cui, Composition-tunable antiperovskite $Cu_xIn_{1-x}NNi_3$ as superior electrocatalysts for the hydrogen evolution reaction, Angew. Chem. Int. Ed. 59 (40) (2020) 17488–17493.
[57] Y. Liu, N. Ran, R. Ge, J. Liu, W. Li, Y. Chen, L. Feng, R. Che, Porous Mn-doped cobalt phosphide nanosheets as highly active electrocatalysts for oxygen evolution reaction, Chem. Eng. J. 425 (2021) 131642.
[58] Z. Abdin, C.J. Webb, E.M. Gray, Modelling and simulation of an alkaline electrolyser cell, Energy 138 (2017) 316–331.
[59] M. Guo, A. Qayum, S. Dong, X. Jiao, D. Chen, T. Wang, In situ conversion of metal (Ni, Co or Fe) foams into metal sulfide (Ni_3S_2, Co_9S_8 or FeS) foams with surface grown N-doped carbon nanotube arrays as efficient superaerophobic electrocatalysts for overall water splitting, J. Mate. Chem. A 8 (18) (2020) 9239–9247.
[60] P. Yan, M. Huang, B. Wang, Z. Wan, M. Qian, H.u. Yan, T.T. Isimjan, J. Tian, X. Yang, Oxygen defect-rich double-layer hierarchical porous Co_3O_4 arrays as high-efficient oxygen evolution catalyst for overall water splitting, J. Energy Chem. 47 (2020) 299–306.
[61] Y. Wang, L. Liu, X. Zhang, F. Yan, C. Zhu, Y. Chen, Self-supported tripod-like nickel phosphide nanowire arrays for hydrogen evolution, J. Mater. Chem. A 7 (39) (2019) 22412–22419.
[62] H. Li, Y. Han, H. Zhao, W. Qi, D. Zhang, Y. Yu, W. Cai, S. Li, J. Lai, B. Huang, L. Wang, Fast site-to-site electron transfer of high-entropy alloy nanocatalyst driving redox electrocatalysis, Nat. Commun. 11 (2020) 5437.
[63] H. Jiang, M. Sun, S. Wu, B. Huang, C.-S. Lee, W. Zhang, Oxygen-incorporated NiMoP nanotube arrays as efficient bifunctional electrocatalysts for urea-assisted energy-saving hydrogen production in alkaline electrolyte, Adv. Funct. Mater. 31 (43) (2021) 2104951.
[64] L. Li, L. Bu, B. Huang, P. Wang, C. Shen, S. Bai, T.-S. Chan, Q.i. Shao, Z. Hu, X. Huang, Compensating electronic effect enables fast site-to-site electron transfer over ultrathin RuMn nanosheet branches toward highly electroactive and stable water splitting, Adv. Mater. 33 (51) (2021) 2105308.
[65] Z. Wu, Y. Zhao, H. Wu, Y. Gao, Z. Chen, W. Jin, J. Wang, T. Ma, L. Wang, Corrosion engineering on iron foam toward efficiently electrocatalytic overall water splitting powered by sustainable energy, Adv. Funct. Mater. 31 (17) (2021) 2010437.
[66] W. Wu, Z. Zhang, Z. Lei, X. Wang, Y. Tan, N. Cheng, X. Sun, Encapsulating Pt nanoparticles inside a derived two-dimensional metal-organic frameworks for the enhancement of catalytic activity, ACS Appl. Mater. Interfaces 12 (2020) 10359–10368.
[67] C. Yang, K. Shen, R. Zhao, H. Xiang, J. Wu, W. Zhong, Q. Zhang, X. Li, N. Yang, Balance effect: A universal strategy for transition metal carbides to enhance hydrogen evolution, Adv. Funct. Mater. 2108167 (2022).
[68] Q. He, D. Tian, H. Jiang, D. Cao, S. Wei, D. Liu, P. Song, Y. Lin, L. Song, Achieving efficient alkaline hydrogen evolution reaction over a Ni5 P4 catalyst incorporating single-atomic Ru Sites, Adv. Mater. 32 (2020) 1906972.
[69] K. Tu, D. Tranca, F. Rodriguez-Hernandez, K. Jiang, S. Huang, Q. Zheng, M. X. Chen, C. Lu, Y. Su, Z. Chen, H. Mao, C. Yang, J. Jiang, H.W. Liang, X. Zhuang, A novel heterostructure based on RuMo nanoalloys and N-doped carbon as an efficient electrocatalyst for the hydrogen evolution reaction, Adv. Mater. 32 (2020) 2005433.
[70] H. Su, S. Song, S. Li, Y. Gao, L. Ge, W. Song, T. Ma, J. Liu, High-valent bimetal Ni_3S_2/Co_3S_4 induced by Cu doping for bifunctional electrocatalytic water splitting, Appl. Catal. B: Environ. 293 (2021), 120225.
[71] J.H. Huang, Y.H. Xie, L. Yan, B.L. Wang, T.Y. Kong, X.L. Dong, Y.G. Wang, Y.Y. Xia, Decoupled amphoteric water electrolysis and its integration with Mn-Zn battery for flexible utilization of renewables, Energ Environ. Sci. 14 (2021) 883–889.
[72] L. Wang, Z. Li, K. Wang, Q. Dai, C. Lei, B. Yang, Q. Zhang, L. Lei, M.K.H. Leung, Y. Hou, Tuning d-band center of tungsten carbide via Mo doping for efficient